Integrated magnetic and kinetic control of advanced tokamak plasmas on DIII-D based on data-driven models

D. Moreau[1], M.L. Walker[2], J.R. Ferron[2], F. Liu[1,a], E. Schuster[3], J.E. Barton[3], M.D. Boyer[3], K.H. Burrell[2], S.M. Flanagan[2], P. Gohil[2], R.J. Groebner[2], C.T. Holcomb[4], D.A. Humphreys[2], A.W. Hyatt[2], R.D. Johnson[2], R.J. La Haye[2], J. Lohr[2], T.C. Luce[2], J.M. Park[5], B.G. Penaflor[2], W. Shi[3], F. Turco[6], W. Wehner[3] and the ITPA-IOS group members and experts

[1] CEA, IRFM, 13108 Saint-Paul-lez-Durance, France
[2] General Atomics, PO Box 85608, San Diego, CA 92186-5608, USA
[3] Lehigh University, Campus Square, Bethlehem, PA 18015, USA
[4] Lawrence Livermore National Laboratory, 7000 East Ave, Livermore, CA 94550, USA
[5] Oak Ridge National Laboratory, PO Box 2008, Oak Ridge, TN 37831, USA
[6] Columbia University, 116th St and Broadway, New York, NY 10027, USA

E-mail: didier.moreau@cea.fr

Abstract

The first real-time profile control experiments integrating magnetic and kinetic variables were performed on DIII-D in view of regulating and extrapolating advanced tokamak scenarios to steady-state devices and burning plasma experiments. Device-specific, control-oriented models were obtained from experimental data using a generic two-time-scale method that was validated on JET, JT-60U and DIII-D under the framework of the International Tokamak Physics Activity for Integrated Operation Scenarios (Moreau *et al* 2011 *Nucl. Fusion* **51** 063009). On DIII-D, these data-driven models were used to synthesize integrated magnetic and kinetic profile controllers. The neutral beam injection (NBI), electron cyclotron current drive (ECCD) systems and ohmic coil provided the heating and current drive (H&CD) sources. The first control actuator was the plasma surface loop voltage (i.e. the ohmic coil), and the available beamlines and gyrotrons were grouped to form five additional H&CD actuators: co-current on-axis NBI, co-current off-axis NBI, counter-current NBI, balanced NBI and total ECCD power from all gyrotrons (with off-axis current deposition). Successful closed-loop experiments showing the control of (a) the poloidal flux profile, $\Psi(x)$, (b) the poloidal flux profile together with the normalized pressure parameter, β_N, and (c) the inverse of the safety factor profile, $\bar{\iota}(x) = 1/q(x)$, are described.

(Some figures may appear in colour only in the online journal)

1. Introduction

The development of hybrid and steady-state operation scenarios with high neutron fluence on ITER implies the control of improved confinement, high-β discharges (β is the ratio of thermal to magnetic pressure), with a large fraction of the plasma current being self-generated by the neoclassical bootstrap effect. Such discharges are obtained in present-day tokamak devices in advanced operation scenarios in which an optimization of some plasma parameter profiles results in a large improvement in normalized fusion performance, at

[a] Permanent address: Southwestern Institute of Physics, PO Box 432, Chengdu, People's Republic of China.

reduced plasma current. In tokamaks, β is usually normalized to the product I_p/aB_T, where I_p is the plasma current, a is the plasma minor radius and B_T is the toroidal magnetic field. Thus, $\beta = \beta_N(I_p/aB_T)$ where β_N is the normalized pressure parameter whose value is a figure of merit for plasma performance. At high β_N, a high-gain fusion burn with extended pulse length (possibly steady state) could be achieved at moderate current in a burning plasma device such as ITER, a major fraction of the toroidal current consisting of the non-inductive bootstrap current. The ongoing research on advanced tokamak (AT) operation scenarios is therefore important for the development of a steady-state tokamak reactor.

Without adequate profile control, AT plasmas are currently obtained in various devices empirically [1–4], either transiently

or for durations that do not exceed the resistive diffusion time. The high plasma performance phase is often limited in duration by transport and magnetohydrodynamic (MHD) phenomena. Extensive work has been dedicated in recent years to the control of MHD instabilities, such as the neoclassical tearing modes (NTMs) or resistive wall modes (RWMs), but simultaneous control of magnetic and kinetic plasma profiles and parameters such as the current density profile, the pressure profile (or at least β_N) and, in ITER, the alpha-particle power, is also essential for the extrapolation of the scenarios to long-pulse or steady-state operation in future tokamaks. In present-day devices, the regulation of plasma parameter profiles is also motivated by the potential gain that it could yield in running stable and reproducible discharges, in order to study the physics of AT plasmas for ITER.

Model-based control of the current density profile using first-principles nonlinear models is being developed [5, 6], with simplifying assumptions or real-time evaluation of a limited number of essential unknown parameter profiles, such as the electron temperature and plasma conductivity. For integrated profile control, involving several magnetic and kinetic parameters and profiles, the first-principles equations governing the evolution of the plasma states become increasingly complex and depend on many uncertain parameters and transport coefficients. This is why an approach based on data-driven models has been initiated on JET [7] and later pursued on JT-60U [8] and DIII-D [8–10], under the framework of the International Tokamak Physics Activity for Integrated Operation Scenarios (ITPA-IOS). It relies on linearized system identification techniques [11] from experimental data (or, if possible, from data obtained from comprehensive and reliable nonlinear simulations) and on singular perturbation control methods [12]. Once an approximate plasma response model to variations of the actuators around a given equilibrium has been identified, an integrated model-based controller can be designed to regulate the plasma state through a global minimization algorithm. Thus, for any chosen set of target profiles, the closest self-consistent plasma state achievable with the available actuators will be tracked. The two-time-scale system identification and plasma control algorithms that are described in [7, 8] and are based on applying the theory of singularly perturbed systems to a set of simplified plasma transport equations will hereafter be referred to by the acronym *ARTAEMIS* (for 'Advanced Real-Time Algorithms based on Empirical Modeling of Integrated Scenarios'). The *ARTAEMIS* algorithm used here to determine the device-specific, control-oriented (approximate) models that are needed for controller design was developed and validated using data from the three tokamaks mentioned above ([8] for specifics of the DIII-D model), and also using data obtained from ITER simulations [13]. It was thus shown that a good approximation of the coupled response of the relevant parameter profiles to variations of specific heating and current drive (H&CD) actuators could be obtained from experimental data where the various actuators were randomly modulated. These data-driven control-oriented models were subsequently used to synthesize various integrated controllers (near-optimal controller [7], mixed sensitivity robust controllers [9, 10]) for the simultaneous control of the current profile and of β_N in the DIII-D high-β_N steady-state scenario, and for current profile

and burn control simulations in the ITER hybrid scenario [13]. The DIII-D plasma control system (PCS) [14] has been upgraded for these experiments and its control capability has been expanded to include the possibility of simultaneously controlling the evolution of one magnetic radial profile such as the internal poloidal magnetic flux, $\Psi(x)$ where x is a radial coordinate defined later, the safety factor, $q(x)$, or its inverse, $\bar{\iota}(x)$, and up to two kinetic profiles (e.g. toroidal rotation and ion temperature) and one scalar parameter such as the normalized pressure parameter, β_N. This paper focusses on the first tests of the *ARTAEMIS* controller [7] in closed-loop control experiments on DIII-D. Sections 2 and 3 describe the choice of the relevant state and input variables, the structure of the reduced state-space models and the main features of the control algorithm. Section 4 provides specific information on the plasma scenario, real-time diagnostics and control actuators used in the experiments. Then in sections 5, 6 and 7, the experimental results for the control of $\Psi(x)$, for the simultaneous control of $\Psi(x)$ and β_N, and for the control of $\bar{\iota}(x)$, respectively, will be described in detail. The general conclusions will be drawn in section 8.

2. Two-time-scale state-space structure of the dynamic plasma models

In a tokamak, the multiple magnetic and kinetic parameter profiles that define the plasma state (poloidal magnetic flux, safety factor, plasma density, velocity, pressure, etc) are known to be strongly and nonlinearly coupled. However, because of this coupling, the parameters and profiles that define a given target plasma state and need to be controlled in real-time to reach the corresponding equilibrium and regulation of the plasma around that state may be reduced to a minimal set of essential ones such as, for example, $\Psi(x)$, $\bar{\iota}(x)$ and β_N. In the model-based control approach followed here, the coupling between magnetic and kinetic plasma parameters and profiles is given more emphasis in the controller synthesis than the nonlinearity of the system. Nonlinear plasma models describing the coupled dynamics of magnetic and kinetic profiles are extremely complex and still too uncertain to be readily integrated in a profile controller design. On the contrary, for a given machine configuration and plasma operation scenario, linear models that approximately reproduce the response of the coupled plasma profiles under variations of given actuators can be found empirically from experimental data, and can be valid in a sufficiently broad vicinity of the plasma equilibrium that needs to be tracked [8]. Nonlinearities that are well identified and understood could nevertheless be taken into account in the future, if needed.

Thus, based on the structure of flux-averaged transport equations, a control-oriented, grey box, state-space plasma model is postulated to consist of a set of strongly coupled linearized plasma response equations that only depend on the normalized radius x and time t [7, 8]:

$$\frac{\partial \Psi(x,t)}{\partial t} = \mathcal{L}_{\Psi,\Psi}\{x\} \cdot \Psi(x,t) + \mathcal{L}_{\Psi,X}\{x\} \cdot X(x,t)$$
$$+ L_{\Psi,P}(x) \cdot P(t) + V_{ext}(t), \tag{1}$$

$$\varepsilon \frac{\partial X(x,t)}{\partial t} = \mathcal{L}_{X,\Psi}\{x\} \cdot \Psi(x,t) + \mathcal{L}_{X,X}\{x\} \cdot X(x,t)$$
$$+ L_{X,P}(x) \cdot P(t). \tag{2}$$

Here, the poloidal magnetic flux function, $\Psi(x,t)$, and a set of kinetic profiles and scalar parameters (such as density, toroidal velocity, ion and electron temperatures, or β_N and, in a burning plasma, the alpha-particle power, P_α), represented by the vector $X(x,t)$, appear as the most natural state variables of the system for our purposes. The system is linearized around an equilibrium state which is called the reference state, and which needs not be known explicitly. The radial variable, x, is defined as $(\Phi/\Phi_{max})^{1/2}$ where $\Phi(x)$ is the toroidal magnetic flux through the poloidal cross-section of a given flux surface, and Φ_{max} its maximum value at the last closed flux surface. In equations (1) and (2), the plasma boundary flux has been subtracted from the total poloidal flux so that $\Psi(1,t) = 0$. All the unknown differential operators $\mathcal{L}_{\alpha,\beta}(x)$ and row vectors $\mathcal{L}_{\alpha,P}$ that characterize the linear response of the system (each of the subscripts α and β stand for Ψ or X) depend on x but are independent of time t, and the input vector $P(t)$ contains the powers from the various available H&CD systems. Note that there is no unknown function of x multiplying $V_{ext}(t)$ in equation (1) and that $V_{ext}(t)$ does not appear in equation (2). These properties stem directly from the definition of the state variables and from the linearization of the flux-averaged transport equations [7]. They have always been used and imposed on the system during the identification process. After projection onto a finite set of radial basis functions (e.g. cubic splines), a lumped-parameter version of the state-space model (equations (1) and (2)) is obtained, in which all distributed variables and unknown operators reduce to vectors and matrices. In the following, the same symbols Ψ and X will be used to denote the functions $\Psi(x,t)$ and $X(x,t)$, respectively, or the vectors $\Psi(t)$ and $X(t)$ whose elements are the coefficients of their respective development on the chosen basis functions. The small constant parameter $\varepsilon(\varepsilon \ll 1)$ represents the typical ratio between the kinetic (energy confinement) and the resistive diffusion time scales. As the order of magnitude of ε is about 0.05 in present-day tokamaks and 0.001 in ITER, we use the theory of singularly perturbed systems both for model identification and controller design [12]. Equations (1) and (2) thus reduce to a slow dynamic model,

$$
\begin{aligned}
\dot{\Psi}(t) &= A_S \cdot \Psi(t) + B_S \cdot U_S(t), \\
X_S(t) &= C_S \cdot \Psi(t) + D_S \cdot P_S(t).
\end{aligned}
\tag{3}
$$

and a fast dynamic model,

$$
\dot{X}_F(t) = A_F \cdot X_F(t) + B_F \cdot P_F(t),
\tag{4}
$$

where the input vector,

$$
U(t) = \begin{bmatrix} P(t) \\ V_{ext}(t) \end{bmatrix},
\tag{5}
$$

and all the kinetic variables contained in $X(t)$ have been split into a slow and a fast component labelled by subscripts S and F, respectively:

$$
U(t) = U_S(t) + U_F(t), \qquad X(t) = X_S(t) + X_F(t), \tag{6}
$$

with

$$
U_S(t) = \begin{bmatrix} P_S(t) \\ V_{ext}(t) \end{bmatrix}, \qquad U_F(t) = \begin{bmatrix} P_F(t) \\ 0 \end{bmatrix}, \tag{7}
$$

The magnetic and kinetic variables are coupled because the evolution of the kinetic functions, $X(x,t)$, is partly governed by the evolution of the magnetic equilibrium through $\Psi(x,t)$. This coupling is represented, in a linearized form, by the C_S matrix. Details concerning this approximation and the identification of a two-time-scale plasma response model from experimental data (grey-box model) can be found in [7, 8]. Then, once the slow and fast models have been identified, a near-optimal two-time-scale controller that minimizes a given cost function to order $O(\varepsilon^2)$ can be synthesized.

3. Model-based near-optimal control design

A near-optimal controller is obtained by applying the theory of singular perturbations to optimal state control, a technique that properly decouples the two time scales when the parameter ε (equation (2)) is sufficiently small [12]. The *ARTAEMIS* near-optimal control algorithm uses two main feedback loops [7]:

(i) A proportional-plus-integral (PI), regulator control loop which, on the basis of the slow model (i.e. on the resistive time scale), drives the system towards the self-consistent equilibrium state that minimizes a given cost function. Thus, the system approaches at best the prescribed target state in the least-squares sense. On the same time scale, the kinetic variables (X_s in equation (3)) follow a quasi-static trajectory that is governed by the evolution of the magnetic variables, $\Psi(t)$, and by the slow evolution of the actuators, $P_S(t)$, subject to this PI control law.

(ii) A fast proportional control loop which ensures the stability of the kinetic variables on the plasma confinement time scale, and regulates their transient behaviour when they are subject to rapid target changes or disturbances. Otherwise, they undergo the slow evolution that is consistent with the slowly evolving plasma configuration towards the target profiles.

Details of the theory can be found in [7]. Assuming that the plasma response is given by equations (1) and (2) and asymptotically reduces to equations (3) and (4) when ε is small, the composite control algorithm provides $U(t) = U_S(t) + U_F(t)$, the best $O(\varepsilon^2)$ solution to the minimization of the cost functional:

$$
\begin{aligned}
J[U(t)] = \int_0^\infty \mathrm{d}t \bigg\{ & [\Delta\Psi^T(t)\,\Delta X^T(t)] \cdot Q \cdot \begin{bmatrix} \Delta\Psi(t) \\ \Delta X(t) \end{bmatrix} \\
& + \alpha_\zeta^2 \zeta^T(t) \cdot \zeta(t) + \Delta U^T(t) \cdot R \cdot \Delta U(t) \bigg\},
\end{aligned}
\tag{8}
$$

where the vectors $\Delta\Psi(t)$ and $\Delta X(t)$ contain the error signals with respect to a target state, $[\Psi_\infty, X_\infty]$, which is assumed to be achievable, here, when the actuator vector, $U(t)$, reaches a steady-state value, U_∞, and the reduced vector, $\Delta U(t) = U(t) - U_\infty$, then vanishes. $\zeta(t)$ is defined as

$$
\zeta(t) = \int_0^t K_\zeta \cdot \begin{bmatrix} \Delta\Psi(t) \\ \Delta X(t) \end{bmatrix} \mathrm{d}\tau,
\tag{9}
$$

and is an extra state vector introduced for integral control [15]. The T superscript is used for vector or matrix transposition. Q and R are positive-definite matrices, K_ζ is an appropriate rectangular scaling matrix that characterizes integral control and α_ζ is a scalar. The first term in the control objective

functional, $J[U(t)]$ (equation (8)), represents the time integral of a quadratic function of the error signals and will cause the $\Psi(x)$ and $X(x)$ profiles to approach their targets in a short time. The second term provides integral control and ensures that the state $[\Psi_\infty, X_\infty]$, which will be defined later as the self-consistent achievable state that is closest to the target, will ultimately be reached without any offset. The final term in the control objective describes the cost of the control action in terms of actuator power. If the model equations (3) through (7) provide a fair approximation of the system dynamics and Q, R and α_ζ^2 are properly tuned, the controller offers a good compromise between performance and cost.

The vectors $U_S(t)$ and $U_F(t)$ that enter the composite control law, $U(t) = U_S(t) + U_F(t)$, are computed in real-time from the equations

$$U_S(t) = \begin{bmatrix} P_S(t) \\ V_{ext}(t) \end{bmatrix} = -\begin{bmatrix} G_S & G_\zeta \end{bmatrix} \cdot \begin{bmatrix} \Delta\Psi(t) \\ \zeta(t) \end{bmatrix}$$
$$= -G_S \cdot \Delta\Psi(t) - G_\zeta \cdot K_\zeta \cdot \int_0^t \begin{bmatrix} \Delta\Psi(t) \\ \Delta X(t) \end{bmatrix} dt, \qquad (10)$$

and

$$U_F(t) = -G_F \cdot X_F(t) = -G_F \cdot [X(t) - C_S \cdot \Psi(t) - D_S \cdot P_S(t)]. \qquad (11)$$

The near-optimal gain matrices, $[G_S \; G_\zeta]$ and G_F, are solutions of two Riccati equations associated with the minimization of $J[U(t)]$ to order $O(\varepsilon^2)$. In fact, the discrete time version of the Riccati equations corresponding to the continuous time system defined in equations (3) and (4) are solved when computing $[G_S \; G_\zeta]$ and G_F, because the controller was implemented in the DIII-D PCS with a discrete sampling time of 20 ms. These calculations can be made off-line once the controller parameters, Q, R and α_ζ^2 have been chosen for a particular discharge, and the controller gain matrices are then uploaded into the PCS together with the reference and target profiles before each shot.

When the target state, $[\Psi_{target}, X_{target}]$, is not achievable with the given set of actuators, an important feature of the algorithm is that, K_ζ can be chosen as an appropriate pseudo-inverse of the static gain matrix, K_∞, of the system, in such a way that integral feedback control drives the system towards the *self-consistent state that is the closest to the target state, achievable with the given actuators*. This state, $[\Psi_\infty, X_\infty]$, and the corresponding steady-state input vector, U_∞, are defined as

$$\begin{bmatrix} \Psi_\infty \\ X_\infty \end{bmatrix} = K_\infty \cdot U_\infty, \qquad U_\infty = K_\zeta \cdot \begin{bmatrix} \Psi_{target} \\ X_{target} \end{bmatrix}, \qquad (12)$$

and by choosing K_ζ as an appropriate pseudo-inverse of our model estimate of K_∞, the functional

$$I_\infty = \int_0^1 dx\{[\Psi_\infty(x) - \Psi_{target}(x)]^2 + \lambda_{kin}^2[X_\infty(x) - X_{target}(x)]^2\}, \qquad (13)$$

where λ_{kin} is a weighting parameter for kinetic control, will be minimized (within the accuracy of the model) when $U = U_\infty$ in steady state.

The order of the controller is the number of first order ordinary differential equations that need be integrated to compute the states, $\zeta(t)$, which are defined in equation (9) and appear in equation (10). The number of these states that are linearly independent, i.e. the controller order, is therefore equal to the rank of K_ζ and is at most equal to the number of actuators. Generally, the condition number of the K_∞ matrix is large, so some combinations of the actuators yield very small steady-state responses compared to others, and target profiles that differ only very slightly could lead to very different requests for U_∞. This may require combinations of large actuator values of opposite signs that would nearly annihilate each other but are outside their allowed range. To possibly avoid actuator saturation and, yet, reach sufficiently small values of I_∞, the K_∞ matrix can be approximated using a truncated singular value expansion, limited to a small number of principal components that correspond to the largest singular values. This lowers the rank of K_∞ (and therefore of its pseudo-inverse K_ζ) and also lowers the norm of U_∞. So, the larger the order of the controller is, the smaller I_∞ can be, but also the larger the risk of saturation is. The controller is also augmented by an anti-windup loop [7] that prevents the winding up of the errors in the integral term of the control law when some actuators saturate, and leaves the nominal closed-loop system unmodified when the actuators are not saturated.

The controllability and observability of the magnetic and kinetic profiles was discussed in [7] and can be inferred from the controllability and observability of the identified two-time-scale system (equations (3) and (4)). The ith eigenvalue, $\lambda_{S,i}$, of the slow system is controllable when

$$\text{Rank}[(\lambda_{S,i} \cdot \text{Id}_{n_x} - A_S) \quad B_S] = n_x, \qquad (14)$$

where n_x is the dimension of the magnetic state vector and Id_{n_x} stands for the identity matrix of order n_x, and the jth eigenvalue, $\lambda_{F,j}$, of the fast system is controllable when

$$\text{Rank}[(\lambda_{F,j} \cdot \text{Id}_{n_z} - A_F) \quad B_F] = n_z, \qquad (15)$$

where n_z is the dimension of the kinetic state vector and Id_{n_z} stands for the identity matrix of order n_z. These tests are made when computing the controller matrices before loading the profile controller data into the PCS. Due to the variety and the rather broad power and current deposition profiles of the chosen actuators, the system was always found to be controllable. Observability is guaranteed by the full knowledge of the controlled profiles provided by a real-time magnetic flux reconstruction on a 65×65 spatial grid from EFIT [16, 17], and on a full set of appropriate measurements.

4. Plasma scenario, diagnostics and specific heating and current drive actuators used for the system identification and profile control experiments

The chosen reference plasma state around which the data-driven models were identified on DIII-D was that of a β_N-controlled AT scenario, at a toroidal magnetic field, $B_T = 1.8$ T in the standard negative direction (i.e. clockwise when viewed from the top of the torus), central plasma density, $n_{e0} \approx 5 \times 10^{19}$ m^{-3} and plasma current, $I_p = 0.9$ MA in the standard positive direction (counter-clockwise when viewed from the top of the torus). The plasma shape was a slightly biased up double null divertor with a safety factor at
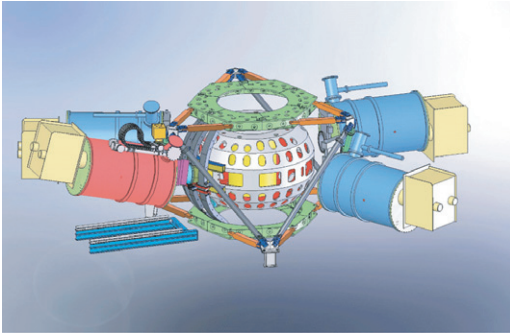
Figure 1. Drawing of the DIII-D tokamak and of its neutral beam system consisting of four beamlines (three for co-current injection and one for counter-current injection), each equipped with two ion sources. The co-current injection beamline located at a toroidal angle of 150° around the torus, shown in red, can be tilted up to 16° with respect to the equatorial plane for off-axis neutral beam current drive.

the plasma edge, q_{95}, equal to 5.8. Since $q(x)$ is infinite at the boundary of a diverted toroidal plasma, q_{95} is defined as the safety factor on a flux surface that contains 95% of the total poloidal flux within the plasma, and is representative of the plasma current, shape and toroidal magnetic field. The scenario had been developed to combine noninductive current fractions near unity with normalized pressure $3.5 < \beta_{\mathrm{N}} < 3.9$, bootstrap current fractions larger than 50%, and a normalized confinement factor, $H_{98(y,2)} \approx 1.5$ [1, 2].

Deuterium neutral beam injection (NBI) and electron cyclotron current drive (ECCD) systems provided the H&CD sources for the system identification and profile control experiments. There are four NBI beamlines on DIII-D, located at toroidal angles of 30°, 150°, 210° and 330° around the tokamak (figure 1). Each beamline is equipped with two ion sources that can be run at different voltages in the range 30–80 kV (some up to 93 kV), and provides two tangential beams, left (L) and right (R), which penetrate the plasma with two different angles of incidence, i.e. with two different tangency radii with respect to the toroidal flux surfaces. The eight beams are labelled 30L, 30R, 150L, 150R, 210L, 210R, 330L and 330R, after their toroidal angular location and relative position in each beamline. In normal operation, when the plasma current is positive, two of these beams (210L and 210R) inject high-energy deuterons in the counter-current direction and the six other beams inject in the co-current direction. In addition, one beamline (beams 150L and 150R) has the capability of being tilted between 0° and 16° with respect to the equatorial plane (figure 1) in order to provide for off-axis co-current injection.

Magnetic profiles were obtained in real-time from a complete equilibrium reconstruction using the real-time EFIT code [16, 17] which solves the Grad–Shafranov equation constrained by edge magnetic sensors and by motional Stark effect (MSE) data that provide information on the poloidal field and current density profiles from a dedicated neutral beam (30L). Kinetic data is obtained from charge exchange recombination spectroscopy (CER) from beam 330R. These two beams were operated in a modulated mode (10 ms on, 10 ms off) at voltages of 80 kV and 74 kV, respectively. Together, they injected in the co-current direction an average

baseline power between 2 and 2.4 MW, depending on the shots, and were not used for control.

In view of future applications involving the simultaneous control of the current density profile together with the electron or ion temperature and/or the toroidal rotation, the six other beams were grouped to form three independent NBI actuators with some decoupling between heating, current drive and torque injection. The grouping can be different depending on the configuration of the 150° beamline, either tilted for off-axis current drive or untilted. At the time when the first system identification and control experiments were performed (sections 5 and 6), the 30R beam was not available and tilting the 150° beamline for off-axis current drive was not possible yet. The three NBI actuators were then made up of:

(i) on-axis co-current NBI power, P_{CO}, provided by the co-current beams with the largest tangency radius, 150L and 330L (note that in sections 5 and 6, the constant average power from the 30L diagnostic beam will also be included in P_{CO} for analysis, as it comes from a beam with about the same characteristics),

(ii) counter-current NBI power, P_{CNT}, provided by the counter-current beam with the largest tangency radius, 210R,

(iii) balanced NBI power, P_{BAL}, provided by two symmetric beams with equal power, and with the smallest tangency radius (one co-current, 150R, the other one counter-current, 210L).

In another experimental campaign (section 7), when both the 30R beam and the off-axis current drive capability became available but 210L was not, another set of NBI actuators was defined as:

(i) on-axis co-current NBI power, P_{CO}, provided by only one co-current beam with the largest tangency radius, 330L (note that in section 7, the constant average power from the 30L diagnostic beam will also be included in P_{CO} for analysis, as it comes from a beam with about the same characteristics),

(ii) counter-current NBI power, P_{CNT}, provided by the counter-current beam with the largest tangency radius, 210R,

(iii) off-axis co-current NBI power, P_{OA}, provided by the two beams with off-axis power deposition, 150L and 150R, with the 150° beamline tilted by 16° with respect to the equatorial plane.

Two additional actuators were used for profile control: the total ECCD power from up to six 110 GHz gyrotrons in a fixed and broad off-axis current drive configuration, P_{EC}, and finally the surface loop voltage, V_{ext}. The use of the surface loop voltage as a natural profile control actuator in the *ARTAEMIS* controllers is guided by the fact that, within our model approximation, the coefficients that determine the response of the controlled variables to $V_{\mathrm{ext}}(t)$ are known and independent of x (section 2, equations (1) and (2)). The surface loop voltage that is requested in real-time during profile control experiments is obtained from the PCS through a separate control system that uses the ohmic coil voltage actuator. The central poloidal field coil (ohmic coil) was therefore used for controlling V_{ext} rather than controlling the total plasma

current, I_p, and I_p was controlled indirectly through the controlled magnetic profiles, e.g. $\Psi(x)$ or $\bar{\iota}(x) = 1/q(x)$. The specific control of $V_{ext}(t)$ was tuned prior to the profile control experiments and, as will be seen in sections 5 to 7, a combined feedforward and feedback control was found to be effective in providing the requested surface loop voltage. This loop voltage control mode of operation, where the total plasma current is not accurately regulated with the ohmic transformer but can be kept floating within some predefined safety bounds, seems suitable for AT scenarios in which a control of the current density profile throughout the plasma cross-section can be at least as important as an accurate control of the total plasma current. Moreover, such scenarios are meant to be ultimately operated in steady state, i.e. at zero loop voltage rather than at a precisely given plasma current. When the controller has brought the plasma sufficiently close to the required state, fully noninductive operation can be readily obtained by letting the weight of V_{ext} vanish with respect to the weight of other actuators in the controller, i.e. by increasing the relevant diagonal R-matrix element in equation (8).

5. Optimal state-feedback control of the poloidal magnetic flux profile

The first closed-loop experiments that were performed to test the *ARTAEMIS* model-based controller will be described now, starting with magnetic profile control only. In the absence of kinetic control, the state-space model contains only the equation of evolution for the poloidal flux profile, $\Psi(x, t)$. The weight parameter, λ_{kin}, equals zero in equation (13), and the control algorithm reduces to conventional optimal control since there is no need for the two-time-scale approximation. In the first experiments, $\Psi(x)$, was controlled from $t = 2.5$ to $t = 6$ s (i.e. starting after a 1 s current flat-top), with four actuators: P_{CO}, P_{BAL} and P_{EC} (with only five gyrotrons) and V_{ext}. All the NBI beamlines were injecting in the equatorial plane so that there was no off-axis NBI power in these experiments, and, in addition, the counter-current NBI actuator was not available ($P_{OA} = P_{CNT} = 0$). Including the 1.2 MW baseline co-current NBI power that was required from beam 30L for real-time MSE measurements into P_{CO}, the allowed ranges for each of the available actuators, P_{CO}, P_{BAL}, P_{EC} and V_{ext} were about 1.2–5.3 MW, 0–4.9 MW, 0.2–2.5 MW and −0.5–0.5 V, respectively, but these limit values were entered manually at the user interface, prior to each shot, and could vary from shot to shot. With powers in megawatts and loop voltage in volts, the square roots of the diagonal R-matrix elements corresponding to P_{CO}, P_{BAL}, P_{EC} and V_{ext} were 0.12, 0.1, 0.2 and 0.4, respectively. Their ratio was chosen on the basis of the inverse available headroom that could be expected on each actuator (difference between the maximum and minimum values), except for V_{ext} that was given a special weight (for example here 2.5 V were given about the same weight as 10 MW of NBI). The elements of the Ψ-vector consisted of the values of $\Psi(x)$ at nine radii ($x = 0.1, 0.2, \ldots 0.9$) and the Q-matrix was chosen in such a way that the quadratic $\Delta \Psi^{T} \cdot Q \cdot \Delta \Psi$ was equal to the integral of $\Delta \Psi(x)^2$ from $x = 0.1$ to 1, assuming the chosen cubic-splines basis functions. K_ζ was a pseudo-inverse of the model steady-state gain matrix, K_∞, defined in section 3 and approximated by its first two

principal components so that the controller order was 2 (the first two singular values of K_∞ were 0.689 and 0.011). In three different experiments, the integral weight parameter, α_ζ, was chosen as 4, 10 and 25, respectively. For these tests, the profile control phase started at $t = 2.5$ s, i.e. 1 s after the end of the initial current ramp-up, and the best controller performance was obtained with $\alpha_\zeta = 25$. This is illustrated in figure 2(a), which shows the time traces of $\Psi(x)$ at $x = 0.1, \ldots 0.9$ in different colours for shot #146416 (the piecewise linear target traces are also represented with the same colours), and on figure 2(b) which shows the $\Psi(x)$ profile at $t = 2.5$ s, 4 s and 6 s, respectively, for the same shot. An overshoot can be observed for all radii before the poloidal flux settles to a final profile that is a good least-squares approximation of the target profile. The time evolution of the actuators is displayed on figure 2(c). It shows almost no saturation, except between $t = 3.5$ and $t = 4.25$ s when the co-current NBI actuator is clamped to its minimum value of 1.2 MW from the MSE diagnostic beam (30L). The actuators nearly reach a stationary state at $t = 5.5$ s. A comparison between the requested and delivered surface loop voltages can be seen on figure 3 and demonstrates the effectiveness of the surface loop voltage control using the ohmic coil actuator. Also shown on this figure is the plasma current which evolves from 0.9 MA before profile control, to 1.1 MA during the profile overshoot, before settling down to a final value of about 1 MA that corresponds to the best approximation of the poloidal flux target profile that can be obtained with the model-based controller. The evolution and successful minimization of the I_∞ quadratic cost function with time can be verified on figure 4 for the three cases when $\alpha_\zeta = 4$ (shot #146410), $\alpha_\zeta = 10$ (shot #146407) and $\alpha_\zeta = 25$ (shot #146416), respectively.

6. Simultaneous near-optimal control of the poloidal flux profile and of the normalized pressure parameter, β_N

Simultaneous control of the poloidal flux profile and of the normalized pressure parameter was performed as a first test of the near-optimal two-time-scale algorithm described in section 3. For this particular application, the kinetic variable, $X(x, t)$, defined in sections 2 and 3 reduces to a single scalar parameter, $\beta_N(t)$, independent of x, and therefore the kinetic vector has only one element. The counter-current NBI actuator, P_{CNT}, became available for some of the experiments described later in this section, so a total of five independent actuators could be used ultimately, with also a little more power in the ECCD actuator since six gyrotrons were operating. The allowed ranges for each of the available actuators, P_{CO}, P_{CNT}, P_{BAL}, P_{EC} and V_{ext} were 1.2–5.3 MW (including the 30L diagnostic beam), 0–2.1 MW, 0–4.4 MW, 0.3–3 MW and −0.5–0.5 V, respectively, and the square roots of the diagonal R-matrix elements were 0.12, 0.2, 0.1, 0.16 and 0.4. The Ψ vector still consisted of the values of $\Psi(x)$ at nine radii ($x = 0.1, 0.2, \ldots 0.9$) and the Q matrix was chosen block-diagonal, such that

$$[\Delta \Psi^{T} \quad \Delta \beta_N] \cdot Q \cdot \begin{bmatrix} \Delta \Psi \\ \Delta \beta_N \end{bmatrix} = \int_0^1 dx \, \Delta \Psi(x)^2 + \lambda_{kin}^2 \Delta \beta_N^2, \quad (16)$$
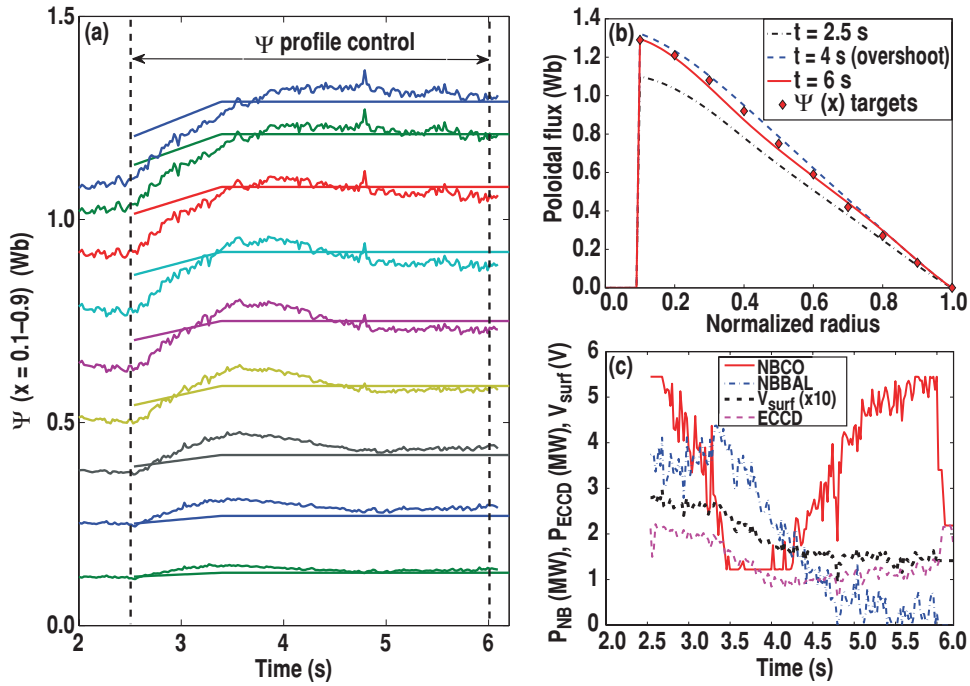
Figure 2. Shot #146416: control of $\Psi(x)$ between $t = 2.5$ s and $t = 6$ s. (a) $\Psi(x)$ at $x = 0.1, 0.2, \ldots 0.9$ versus time and target traces (piecewise linear). (b) $\Psi(x)$ profile at $t = 2.5$ s, 4 s and 6 s and target profile (diamonds). (c) Actuator values, P_{CO} (solid, red), P_{BAL} (dotted–dashed, blue), P_{EC} (dashed, magenta) and V_{ext} (x10, dotted, black) versus time (the co-current NBI power shown here includes a constant baseline power of 1.2 MW required for MSE).

i.e. almost as before except for an additional diagonal element equal to λ_{kin}^2 corresponding to the weight on the control of β_N in the objective of minimizing

$$I_\infty = \int_0^1 dx [\Psi_\infty(x) - \Psi_{target}(x)]^2 + \lambda_{kin}^2 [\beta_{N,\infty} - \beta_{N,target}]^2. \quad (17)$$

As in section 3, $[\Psi_{target}, \beta_{N,target}]$ represents the target state, and $[\Psi_\infty, \beta_{N,\infty}]$ represents, according to the model, the state which is the closest to the target state that can be reached in closed-loop, while the actuator vector, $U(t)$, reaches its final steady-state value, U_∞. Based on the relative magnitude of the steady-state gains of the model, the weight on β_N control was chosen as $\lambda_{kin} = 0.3$. Now, the five singular values of the steady-state gain matrix, K_∞, were 0.929, 0.085, 0.016, 0.006 and about 10^{-4}. Only three principal components of K_∞ were retained in the calculation of its pseudo-inverse, K_ζ, for integral control, and α_ζ was chosen equal to 10. For the first tests, only the same four actuators as for the control of the poloidal flux profile (section 5) were available. With the same poloidal flux target profile as for shot #146416 and with $\beta_{N,target} = 2.07$, the simultaneous control of $\Psi(x)$ and β_N was switched on from $t = 2.5$ to $t = 6$ s. With the chosen parameters, this controller of order 3 showed good performance with practically no actuator saturation. This is illustrated in figure 5 which shows the time traces of $\Psi(x)$ at $x = 0.1, 0.2, \ldots 0.9$ in different colours (figure 5(a)) and of β_N (figure 5(b)), for shot #146422. As in section 5 (shot #146416) when the controller parameters were tuned to reach a steady current profile around $t = 4.5$ s, an overshoot can be observed on the poloidal flux control and the plasma current rises slightly above its final value before ramping down to equilibrium. On the contrary, β_N was nearly on its target
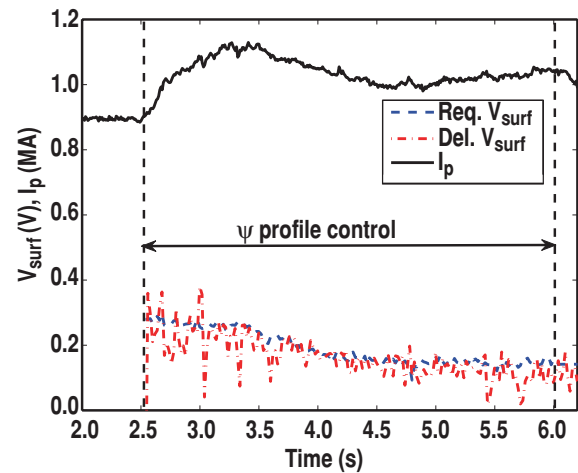

Figure 3. Shot #146416: control of $\Psi(x)$ between $t = 2.5$ s and $t = 6$ s. Plasma current versus time (solid, black), requested surface loop voltage (dash, blue) and delivered surface loop voltage, filtered (dotted–dashed, red).

trace only about 100 ms after control was switched on, and good tracking was achieved until the end of the control phase. The time evolution of the H&CD actuators, P_{CO}, P_{BAL} and P_{EC} is displayed on figure 5(c). One can see that they have not reached steady state yet at the end of the control phase ($t = 6$ s) although the controlled variables are almost steady and sufficiently close to their respective targets. The evolution of the plasma current towards its final value of about 1 MA can be seen on figure 6, together with a comparison between the requested and delivered surface loop voltages.

Tailoring the current density profile during the plasma current ramp-up phase, through the choice of an optimal ramp-up rate and the combined effects of the ohmic drive,
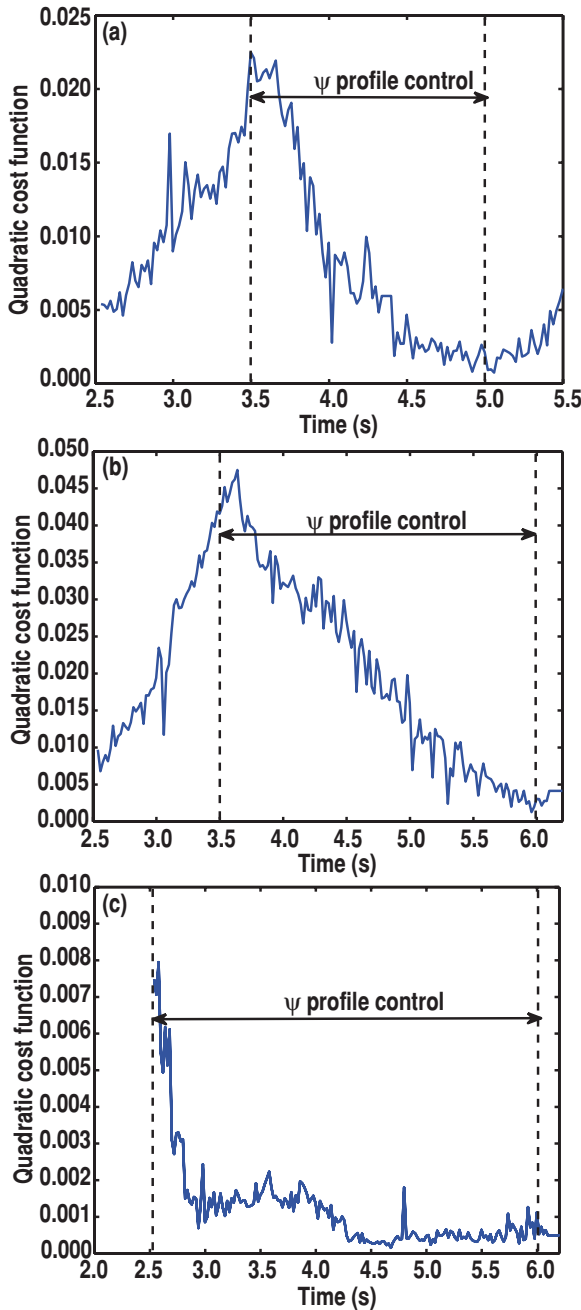
Figure 4. Evolution of the cost function, I_∞, during poloidal flux profile control with various integral control parameters. (*a*) Shot #146410: control between $t = 3.5$ s and $t = 6$ s with $\alpha_\zeta = 4$. (*b*) Shot #146407: control between $t = 3.5$ s and $t = 5$ s with $\alpha_\zeta = 10$. (c) Shot #146416: control between $t = 2.5$ s and $t = 6$ s with $\alpha_\zeta = 25$.

electron heating and noninductive current generation, is an essential ingredient of the AT operation scenarios, that leads to improved confinement and stability. The development of real-time profile control during the current ramp-up phase could therefore constitute an important progress for running stable and reproducible AT discharges despite the significant variations of the plasma parameters that are observed after plasma initiation, X-point formation and H-mode transition. In discharges used for profile control testing, the X-point configuration was formed at $t \approx 0.3$ s and the plasma transition to H-mode occurred at $t = 0.5$ s. Therefore, during experiments subsequent to shot #146422, the starting time of

the $\Psi(x)$ profile and β_N control phase was moved forward, from 2.5 s (in shot #146422) to 1.5 s (at the end of ramp-up, when $I_p = 0.9$ MA), then to 1 s (during ramp-up, when $I_p = 0.75$ MA), and finally to 0.5 s (during ramp-up, when $I_p = 0.6$ MA). In the last two cases, control was deliberately switched off at $t = 5.5$ s because of the limited pulse length of the gyrotrons and beams at high power. These experiments were executed after the counter-current 210R beam became available and they used five actuators (P_{CO}, P_{CNT}, P_{BAL}, P_{EC} and V_{ext}). The controller performed well, despite the fact that the data-driven model was identified using only data after 2.5 s [8], i.e. after the plasma equilibrium had relaxed from the initial current ramp-up phase through resistive diffusion, at $I_p = 0.9$ MA. Figure 7 displays the result for shot #146463 in which the profile controller was turned on at $t = 1$ s and off at $t = 5.5$ s. Figure 7(*a*) shows the time traces of $\Psi(x)$ at $x = 0.1, 0.2, \ldots 0.9$ tracking the nine piecewise linear target traces and figure 7(*b*) shows the $\Psi(x)$ profile at $t = 0.5, 2.4$ and 5 s. As in the previous shots, the $\Psi(x)$ profile slightly overshoots the target profile in the interval $t = 2.5$–4 s. Figure 7(*c*) shows several time traces: β_N tracking its flat-top target value of 2.5, the plasma current reaching a maximum value of 1.2 MA at $t = 2.3$ s and floating slightly above 1 MA between $t \approx 4$ s and $t = 5.5$ s, and a rotating $m/n = 2/1$ MHD mode (NTM) as measured by the toroidal and poloidal Mirnov probe arrays. Despite the presence of the $m/n = 2/1$ mode from $t = 2.3$ s to the end, simultaneous $\Psi(x)$ and β_N control was achieved and a nice regulated steady state was obtained between $t = 4$ s and $t = 5.5$ s. It must be noted that the balanced injection actuator, P_{BAL}, made up of beams 150R and 210L was saturated between $t = 2.1$ s and $t = 4$ s and the counter-current NBI and ECCD actuators were saturated between $t = 2.2$ s and $t = 2.6$ s ($P_{CNT} = P_{CNT,max} = 2$ MW, $P_{BAL} = P_{BAL,max} = 4.4$ MW, $P_{EC} = P_{EC,min} = 0.3$ MW). In the next shot, #146464, with the earliest switch-on time (0.5 s), the plasma current was also successfully ramped up by the profile controller (figure 8), starting from $I_p = 0.6$ MA at $t = 0.5$ s to about 1.07 MA at $t \approx 1.3$ s and $\Psi(x)$ also approached the final target profile slightly after 2 s. As in the previous experiment, the β_N target was constant and equal to 1.5 until $t = 1.5$ s with a linear ramp to 2.5 between 1.5 s and 2 s. This target trace was successfully tracked until β_N reached 2.2 at $t \approx 1.9$ s (figure 8(*a*)). Then β_N dropped to about 1.9, in the same fashion as in figure 7(*c*) around $t \approx 2.5$ s, and the same three actuators reached saturation (figure 8(*b*)). At $t = 1.89$ s, an $m/n = 2/1$ NTM was triggered but, in this discharge, it locked at $t = 1.95$ s. The intrinsic error field had fully penetrated by 2.05 s, with subsequent loss of H-mode, and the locked mode then induced a disruption that terminated the discharge prematurely at $t = 2.35$ s while P_{CNT}, P_{BAL} and P_{EC} were still saturated. The time evolution of the requested and achieved loop voltages are shown on figure 8(*c*) together with a comparison between the plasma current evolution in this discharge and in the previous one where good control was recovered after the onset of the $m/n = 2/1$ MHD activity.

The choice of the controlled variables that was made here, namely the poloidal flux profile and the normalized pressure parameter, was the simplest one for the first tests of a two-time-scale state-feedback controller. It stems directly from the structure and the robustness (for a particular plasma scenario)
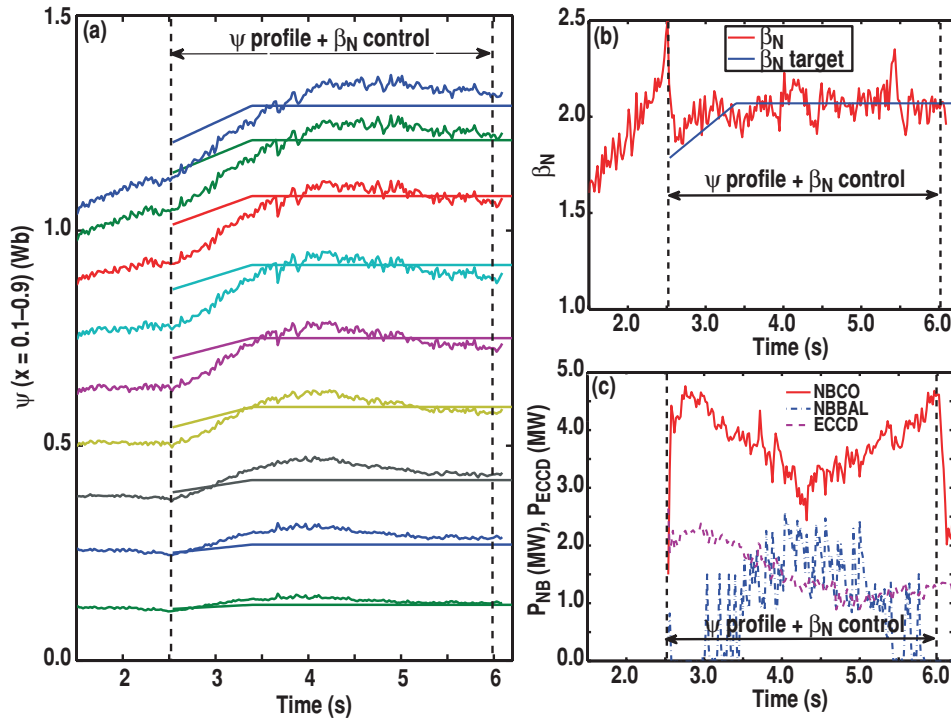
Figure 5. Shot #146422: simultaneous control of $\Psi(x)$ and β_N between $t = 2.5$ s and $t = 6$ s. (*a*) $\Psi(x)$ at $x = 0.1, 0.2, \ldots 0.9$ versus time and target traces (piecewise linear). (*b*) β_N versus time (solid, red) and target trace (piecewise linear, blue). (*c*) H&CD actuator values, P_{CO} (solid, red), P_{BAL} (dotted–dashed, blue) and P_{EC} (dashed, magenta) versus time (the co-current NBI power shown here includes a constant baseline power of 1.2 MW required for MSE).
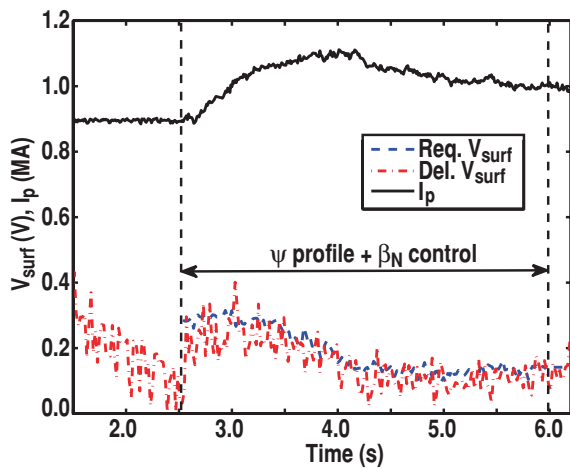

Figure 6. Shot #146422: simultaneous control of $\Psi(x)$ and β_N between $t = 2.5$ s and $t = 6$ s. Plasma current versus time (solid, black), requested surface loop voltage (dashed, blue) and delivered surface loop voltage, filtered (dotted–dashed, red).

of the model identified in [8] and described in section 2. However, as will be discussed in detail in section 7, the safety factor profile, $q(x)$, which is closely linked to the poloidal flux profile, is an important physical quantity that governs MHD stability in tokamak plasmas. At this stage, it is therefore worth measuring the impact on the q-profile of the residual errors between the target and actual $\Psi(x)$ profiles. For this purpose, the values of the $\Psi(x)$ targets shown on figure 7(*b*) were translated into $q(x)$ values by using both the actual toroidal magnetic flux measured in shot #146463 between $t = 4$ s and $t = 5.5$ s, and the cubic-spline interpolation, $\Psi_{target}(x)$, assumed in the definition of the control objective

(equation (17)). In principle, these values of $q(x)$ slightly depend on time through the toroidal magnetic flux, but these variations are in fact negligible. The comparison between the q-profile deduced from $\Psi_{target}(x)$ and the actual q-profiles (deduced from EFIT) during the $\Psi(x)$ overshoot ($t = 2.4$ s) and then between $t = 4$ s and $t = 5.5$ s, is shown on figure 9 (at the time when this experiment was performed, however, the radial derivative of $\Psi_{target}(x)$—and hence of $q(x)$—at the boundaries of the interpolation window, $x = 0.1$ and 1, were not meaningful and are not shown). One can thus get a better intuition about the relationship between the uncertainties on the poloidal flux profile and the safety factor profile, and anticipate on the added value of genuinely controlling the safety factor in real-time, by defining control objectives that are directly related to $q(x)$ (section 7).

Finally, although integrated profile control will be necessary for achieving and maintaining stable gradients in steady-state AT plasmas, these results also point to the importance of direct MHD stability control, and in particular NTM control, during the transient evolution of the plasma current and pressure profiles towards steady state. Research on this topic has been actively pursued during recent years, and substantial progress has been made. For example, accurate tracking and efficient stabilization of the mode with localized ECCD has been shown on DIII-D [18]. With an adequate actuator sharing algorithm, the techniques that are being developed for NTM control and profile control may have to complement each other in the future, in order for fully non-inductive operation at high β_N and with a large bootstrap current fraction to become routinely achieved on DIII-D. In a burning plasma (e.g. in ITER or in a power plant), however, the relative 'strength' of the H&CD actuators will be small
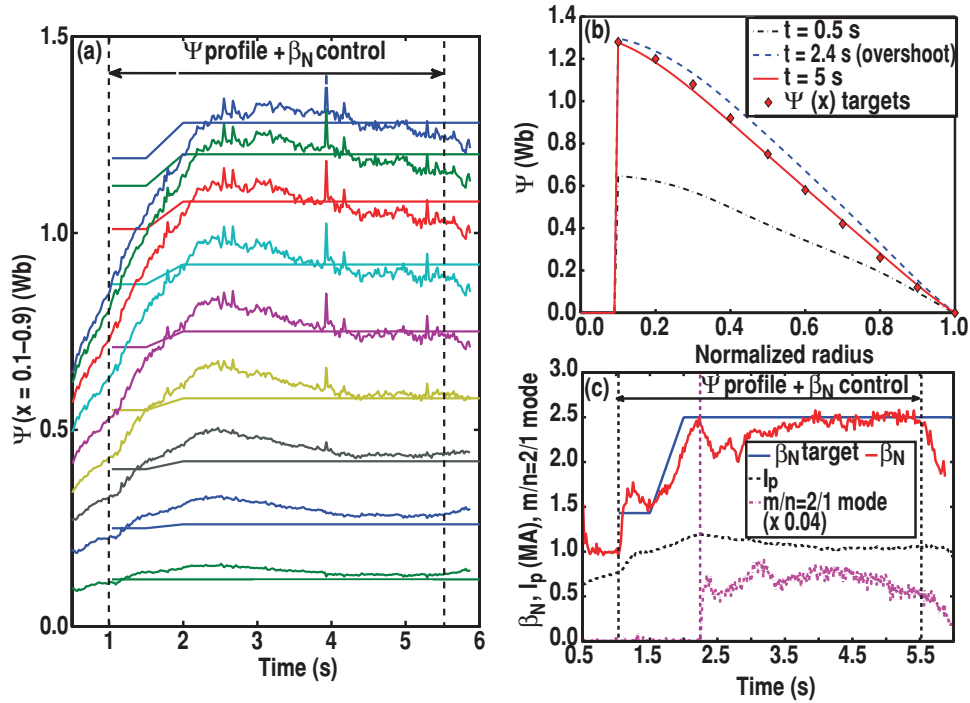
Figure 7. Shot #146463: simultaneous control of $\Psi(x)$ and β_N between $t = 1$ s and $t = 5.5$ s. (*a*) $\Psi(x)$ at $x = 0.1, 0.2, \ldots 0.9$ versus time and target traces (piecewise linear). (*b*) $\Psi(x)$ profile at $t = 0.5$ s, 2.4 s and 5 s and target profile (diamonds). (*c*) β_N (solid, red), target β_N (piecewise linear, blue), plasma current (dotted, black) and $m/n = 2/1$ MHD mode amplitude (dotted–dashed, magenta).

compared to the heating and bootstrap current generated by the 3.5 MeV alpha-particles. MHD instability avoidance may then be a key to a successful strategy for steady-state operation, as it is unlikely that the available actuators will be powerful enough to return the plasma to the desired state after an MHD event. Ideally, then, simultaneous magnetic (including the safety factor) and kinetic profile control, should also provide a tool for moving the plasma evolving towards instability away from it. Knowing the optimal profile shapes and trajectories, in real-time, will thus be important for updating the profile target waveforms.

7. Optimal feedback control of the safety factor profile

In toroidal magnetic confinement devices such as tokamaks, the safety factor is a so-called flux function (i.e. it is constant on a given flux surface and therefore, at a given time, it depends only on x), that is defined as $q(x) = -d\Phi(x)/d\Psi(x)$. When the plasma current is mostly driven inductively and has fully diffused, the safety factor is generally a monotonically increasing function of x. It varies from $q(0) \approx 1$ on the magnetic axis to a value that ranges between about 3 and 10 in the very edge of the plasma (inversely depending on the total plasma current) in plasmas bounded by a limiter, and rapidly increases to infinity at the plasma boundary in diverted plasmas in which the last closed magnetic flux surface is a separatrix. The particular flux surfaces where this parameter is a low-order rational number are the loci of resonances for unstable MHD perturbations that can lead to the formation of large magnetic islands with degradation of plasma confinement, and even sometimes to plasma disruptions. The magnetic shear, which is related to the radial derivative of the safety factor, is also an important parameter for the onset of microturbulence and

anomalous plasma transport. As a matter of fact, steady-state, noninductively driven AT plasmas take most of their benefit from the shaping of the safety factor profile during the current ramp-up phase and the sustainment (at least for a few resistive diffusion times in present tokamaks) of a magnetic equilibrium with an elevated $q(x)$ profile, e.g. with $q(x)$ larger than 1.5 or 2 in the core, and a weak (or slightly negative) magnetic shear in the inner half of the plasma. To reliably achieve such equilibria and to extend the improved performance of AT scenarios to steady state, it would therefore be of great value to control, in real-time, not necessarily the poloidal flux profile as was shown in sections 5 and 6, but rather the safety factor profile or both. It is of course more demanding in terms of modelling and of real-time measurements and control because it depends on the radial derivative of the poloidal flux. Moreover, the target $q(x)$ profiles that are required are not consistent with those that are naturally obtained through the resistive diffusion of any inductively driven current source while the inductive drive is, by far, the most efficient actuator that is available on tokamaks.

In the experiment described below, the safety factor profile was controlled through its inverse, $\bar{\iota}(x) = 1/q(x) = \iota(x)/(2\pi)$, where $\iota(x)$ refers to the rotational transform and is defined, in toroidal plasmas, as the poloidal angle subtended during a single toroidal transit of the field lines on a particular flux surface, expressed in radians. Controlling $\bar{\iota}(x)$ is a natural choice due to the inverse dependence of $q(x)$ with respect to the poloidal flux and current density profiles, and therefore with respect to the control actuators. The postulated structure of equations (1) and (2) and the choice of the model states $[\Psi(x, t), X(x, t)]$ and inputs $[P(t), V_{\text{ext}}(t)]$ was indeed based upon linear relationships between beam-driven or wave-driven currents and injected powers through current drive efficiencies, and between the ohmic current density and the surface loop voltage through Ohm's law ([7], appendix A1). In order
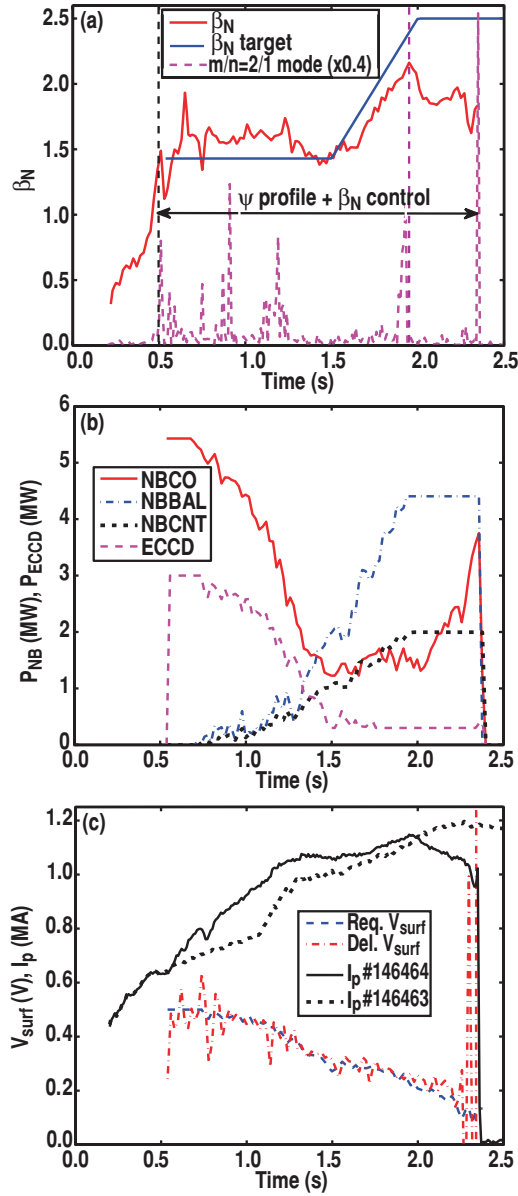
Figure 8. Shot #146464: simultaneous control of $\Psi(x)$ and β_N between $t = 0.5\,$s and $t = 2.4\,$s. (*a*) β_N (solid, red), β_N target (piecewise linear, blue) and $m/n = 2/1$ MHD mode amplitude (dashed, magenta). (*b*) H&CD actuator values in MW, P_{CO} (solid, red), P_{CNT} (dotted, black), P_{BAL} (dotted–dashed, blue) and P_{EC} (dashed, magenta), versus time (the co-current NBI power shown here includes a constant baseline power of 1.2 MW required for MSE). (*c*) Plasma current (MA) versus time (solid, black), requested surface loop voltage in volts (dashed, blue) and delivered surface loop voltage, filtered (dotted–dashed, red). For comparison, the dotted black trace represents the plasma current in shot #146463.

to control $\bar{\iota}(x)$, an additional equation relating the output variable, $\bar{\iota}(x)$, to the model states must be introduced. With our definition of the normalized radius, $x = (\Phi/\Phi_{max})^{1/2}$, this equation reads:

$$
\bar{\iota}(x, t) = -\left[\frac{\partial \Psi(x, t)}{\partial x}\right] \cdot \left[\frac{\partial \Phi(x, t)}{\partial x}\right]^{-1}
$$
$$
= -\frac{1}{2\Phi_{max}(t)}\left[\frac{1}{x}\frac{\partial \Psi(x, t)}{\partial x}\right], \qquad (18)
$$

and $\Phi_{max}(t)$ is known from the real-time magnetic equilibrium reconstruction that provides the current profile data. Therefore,
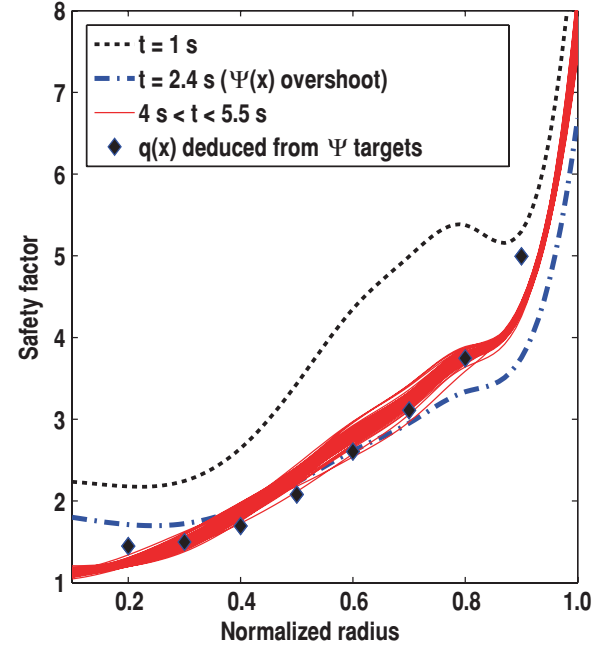

Figure 9. Shot #146463: safety factor profile evolution during the simultaneous control of $\Psi(x)$ and β_N displayed on figure 7. The figure shows $q(x)$ at $t = 1\,$s (dotted, black, start of control), 2.4 s (dotted–dashed, blue, during the $\Psi(x)$ overshoot), and every 20 ms between $t = 4\,$s and $t = 5.5\,$s (solid, red). The $q(x)$ values at $x = 0.2, 0.3, \ldots 0.9$, deduced from the $\Psi(x)$ target profile and from the toroidal flux profile reconstructed by EFIT are also shown for comparison (diamonds).

the approximate finite development

$$
\Psi(x, t) \approx \sum_{k=1}^{N} \Psi_k(t) \cdot a_k(x), \qquad (19)
$$

in terms of the components, Ψ_k of the Ψ-vector and a set of cubic splines, $a_k(x)$, that led to the discrete model equations (3) and (4), readily provides an approximation for $\bar{\iota}(x, t)$,

$$
\bar{\iota}(x, t) \approx -\frac{1}{2\Phi_{max}(t)} \sum_{k=1}^{N} \Psi_k(t) \cdot \alpha_k(x), \qquad (20)
$$

in terms of a finite development on a different set of basis functions, $\alpha_k(x) = (1/x)(da_k/dx)$, using the same coefficients as the $\Psi(x, t)$ development. When the magnetic axis ($x = 0$) is included in the radial interval where the profiles are to be controlled, the basis functions, $a_k(x)$, used to approximate $\Psi(x)$ must satisfy a regularity condition at $x = 0$, namely that their first derivative vanishes. This ensures that the new basis functions, $\alpha_k(x)$, used to approximate $\bar{\iota}(x)$, are finite at $x = 0$ and that the approximate rotational transform and safety factor are defined and finite on the magnetic axis, as their physical counterpart is. Once a sufficiently accurate model has been identified for the dynamics of $\Psi(x, t)$ through the Ψ-vector and the $a_k(x)$ basis functions, there is in principle no need for identifying a specific model describing the dynamics of the $\bar{\iota}(x, t)$ profile. Based on the linear relationship between $\Psi(x, t)$ and $\bar{\iota}(x)$ (equation (18)), optimal control of the $\bar{\iota}(x)$ profile (or near-optimal simultaneous control of $\bar{\iota}(x)$ and of additional kinetic variables with a two-time-scale algorithm) can also be achieved through the state control of the Ψ-vector,
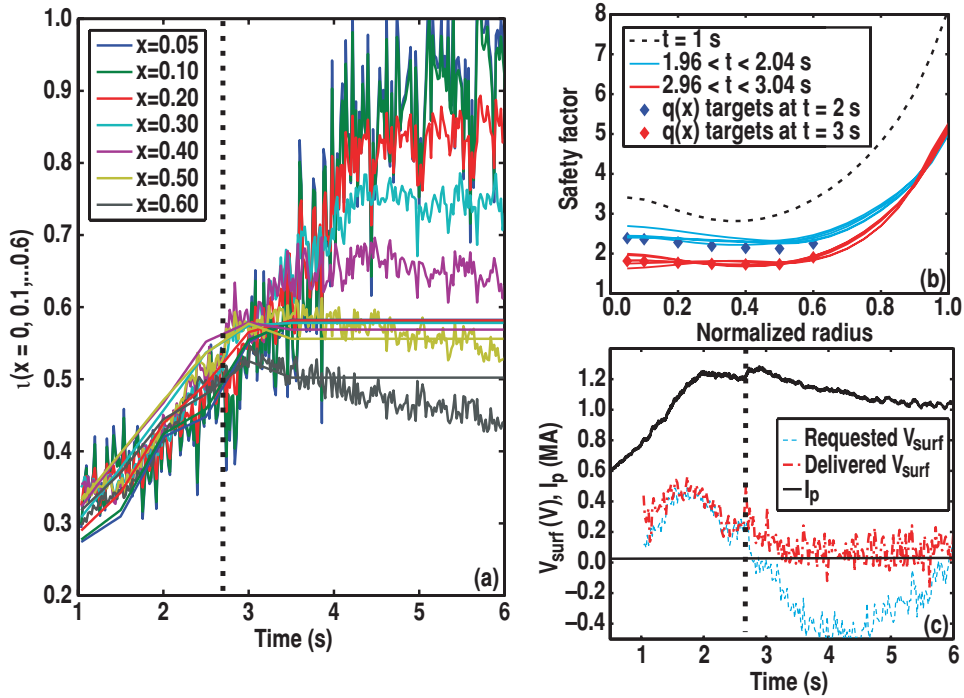
11

Figure 10. Shot #150083: control of $\bar{\iota}(x)$ and therefore $q(x)$ in the interval $0 \leqslant x \leqslant 0.6$ starting at $t = 1$ s, during current ramp-up. (*a*) $\bar{\iota}(x)$ at $x = 0.05, 0.1, 0.2, \ldots 0.6$ versus time and target traces (piecewise linear). A vertical line at 2.7 s shows the time when the ohmic coil current crossover failed, resulting in the loss of V_{ext} control and, subsequently, of $\bar{\iota}(x)$ and $q(x)$ control. (*b*) q-profiles at $t = 1$ s (dashed, black), 2 s (cyan) and 3 s (red) and target values at $t = 2$ s (blue diamonds) and 3 s (red diamonds). (*c*) Plasma current (solid, black), requested surface loop voltage (dashed thin, cyan) and delivered surface loop voltage, filtered (dotted–dashed, red) versus time.

with an appropriate objective that forces the $\bar{\iota}(x)$ profile to reach the closest least-squares approximation of a given $\bar{\iota}(x)$ target profile, $\bar{\iota}_{target}(x)$, within the constraints of the actuators. Hence, introducing the appropriate scalar products of the new basis functions, $\alpha_k(x)$, the Q matrix will be defined here in such a way that

$$[\Delta\Psi^{\mathrm{T}} \quad \Delta\beta_{\mathrm{N}}] \cdot Q \cdot \begin{bmatrix} \Delta\Psi \\ \Delta\beta_{\mathrm{N}} \end{bmatrix} = \int_0^1 \mathrm{d}x[\Delta\bar{\iota}(x)^2 + \lambda_{\mathrm{kin}}^2 \Delta X(x)^2],$$
(21)

and, similarly, the K_ζ matrix will be chosen so that the steady-state control objective amounts to minimizing

$$I_\infty = \int_0^1 \mathrm{d}x\{[\bar{\iota}_\infty(x) - \bar{\iota}_{target}(x)]^2$$
$$+ \lambda_{\mathrm{kin}}^2 [X_\infty(x) - X_{target}(x)]^2\}.$$
(22)

Here, as before, $[\bar{\iota}_{target}, X_{target}]$ represents the target state, and $[\bar{\iota}_\infty, X_\infty]$ represents, according to the model, the state which is the closest to the target state that can be reached in closed-loop, while the actuator vector, $U(t)$, reaches its final steady-state value, U_∞.

These extensions were implemented in the *ARTAEMIS* controller and first experiments were attempted for the control of $\bar{\iota}(x)$, i.e. with $\lambda_{\mathrm{kin}} = 0$. When these experiments were carried out, the 150° co-current beamline was tilted to an angle of 16° upwards with respect to the previous horizontal injection, in order to allow for off-axis NBI and to broaden the family of current profiles accessible to the AT steady-state scenarios. The control actuators thus included off-axis NBI power, P_{OA}, together with P_{CO}, P_{CNT}, P_{EC} and V_{ext}, but no balanced injection ($P_{BAL} = 0$, see section 4). However, the dynamic response of the plasma profiles to the off-axis beams

was only crudely estimated from some open-loop experimental data obtained prior to the control experiment, with limited dynamics. In addition, the magnetic field, 1.7 T, was lower and its direction was reversed (to increase the current drive efficiency of the off-axis beams) compared to what it was (-1.8 T) when the model had been identified. The square roots of the diagonal R-matrix elements corresponding to P_{CO}, P_{OA}, P_{CNT}, P_{EC} and V_{ext} were chosen as 0.1, 0.05, 0.08, 0.06 and 0.05, respectively. The $\bar{\iota}(x)$ target profile corresponded to a broad flat q-profile between $x = 0$ and $x \approx 0.6$, with a minimum value, $q_{min} = 1.7$, that had been achieved previously in this plasma configuration. The integration limits in equations (21) and (22) were modified to limit the radial control window for $\bar{\iota}(x)$ to the interval $0 \leqslant x \leqslant 0.6$, and the control phase began at $t = 1$ s, during current ramp-up, and was programmed to end at $t = 6$ s (figure 10). However, it was found during these tests that starting control at $t \approx 1$ s or before requires a special adjustment of the primary circuit pre-magnetization so that the critical crossover of the ohmic coil current from positive to negative occurs before the switchover from I_p control to V_{ext} control. A second crossover, that would be needed if the loop voltage request from the *ARTAEMIS* profile controller happens to become negative just after the first crossover, is not technically possible at present. In such an occurrence, the ohmic coil current is clamped at zero. In the experiment described here, the primary circuit pre-magnetization was indeed too large for the crossover to be fully completed before the profile control phase began. The current in the ohmic coil changed sign only at $t \approx 2.7$ s (i.e. during the V_{ext} control phase). At that time, the request on V_{ext} became negative, the ohmic coil current was clamped and therefore, from this point on, the request on V_{ext} could not be met anymore (figure 10(*c*)). Nevertheless, the controller

satisfactorily tracked the $\bar{\iota}(x)$ target profile from $t = 1\,\mathrm{s}$ until $t \approx 3.1\,\mathrm{s}$, as shown on figures 10(*a*) and 10(*b*). During that time, the plasma current rose up to reach about 1.2 MA at $t \approx 2\,\mathrm{s}$, and remained roughly constant afterwards. The q-profile obtained in real-time by the EFIT magnetic equilibrium code is displayed on figure 10(*b*) at $t = 1\,\mathrm{s}$, 2 s and 3 s together with the target profiles at $t = 2\,\mathrm{s}$ and 3 s. Subsequently, V_{ext} was clamped near zero, both P_{CO} and P_{OA}, the on-axis and off-axis co-current NBI actuators, saturated at their maximum values, and control of $\bar{\iota}(x)$ was lost. Nevertheless, without any feedforward command except the constant reference powers and surface voltage around which the model was linearized ($P_{\mathrm{CO.ref}} = 3.28\,\mathrm{MW}$, $P_{\mathrm{OA.ref}} = 0$, $P_{\mathrm{CNT.ref}} = 0$, $P_{\mathrm{EC.ref}} = 1.38\,\mathrm{MW}$ and $V_{\mathrm{ext.ref}} = 0.14\,\mathrm{MW}$), the *ARTAEMIS* feedback controller was effective in achieving plasma current ramp-up while tracking successfully the given safety factor target profiles.

8. Conclusion

A generic method for integrated magnetic and kinetic profile control based on semi-empirical data-driven models is being experimentally tested on DIII-D, in order to possibly regulate and improve the performance and reproducibility of AT plasmas, and to extend the corresponding scenarios to long-pulse or steady-state operation in superconducting tokamaks.

Dynamical state-space models have been identified from experimental data obtained during dedicated modulation experiments. In the absence of experimental data (e.g. for future devices such as ITER), such control-oriented, state-space models can also be identified from simulated data obtained from semi-empirical predictive transport codes. They could provide, for integrated control design purposes, a suitable alternative to first-principle plasma models that become increasingly complex and uncertain when the coupled dynamics of several magnetic and kinetic parameter profiles is to be predicted.

In this work, both the model identification and the control techniques use singular perturbation methods in order to take advantage of the small ratio, ε, between the confinement and resistive diffusion time scales (two-time-scale approximation). As far as system identification is concerned, these methods were shown previously to yield reduced-order state-space models which could fairly reproduce the slow and the fast dynamics of the magnetic and kinetic parameter profiles, in a broad vicinity of a reference equilibrium plasma state. A control algorithm based on the same approximation has been implemented on DIII-D after the PCS had been upgraded and its control capability had been expanded to include the possibility of simultaneously controlling the evolution of several magnetic and kinetic plasma parameters and profiles. For magnetic control only, it uses optimal control theory. For integrated magnetic and kinetic control, it yields an $O(\varepsilon^2)$ approximation of optimal control (near-optimal control) where ε is the small ratio between the energy confinement and the resistive diffusion time scales. Since, with a given set of actuators, the family of achievable steady-state plasma equilibria cannot be known with precision in advance, the plasma target state which is aimed at in a control experiment may not be a self-consistent equilibrium state. The *ARTAEMIS*

algorithm allows in principle the controller to reach the closest self-consistent state that is achievable with the given actuators, as defined by the least-squares minimization of a quadratic integral error.

In these experiments, the profile control actuators were the surface loop voltage, V_{ext}, and a subset of five other independent H&CD sources: on-axis co-current NBI, off-axis co-current NBI, counter-current NBI, balanced NBI, and ECCD in a fixed off-axis current drive configuration. The central poloidal field coil (ohmic coil) was used for controlling V_{ext}, and the total plasma current, I_{p}, was controlled indirectly through the controlled magnetic profile which was either the poloidal flux, $\Psi(x)$, or the inverse of the safety factor, $\bar{\iota}(x) = 1/q(x)$. After some tuning, a combined feedforward and feedback control of the surface loop voltage through the ohmic coil voltage was found to be effective in providing the $V_{\mathrm{ext}}(t)$ waveforms requested by the profile controller in real-time.

Closed-loop feedback control of the poloidal flux profile was first demonstrated while some of the parameters that define the control objective were varied. Then, the control phase was extended from $t = 2.5\,\mathrm{s}$ to $t = 6\,\mathrm{s}$ and good tracking of the nine $\Psi(x)$ time-varying target traces ($x = 0.1, 0.2, \ldots 0.9$) was achieved until the end of the control phase. Plasma equilibrium was reached around $t = 4.5\,\mathrm{s}$ consistently with the resistive diffusion time scale.

In another set of experiments, simultaneous control of the poloidal flux profile and the normalized pressure parameter, β_{N}, was experimentally demonstrated using the two-time-scale near-optimal algorithm. Here the control phase started earlier to include part of the current ramp-up phase. Again, good tracking of the nine $\Psi(x)$ time-varying target traces ($x = 0.1, 0.2, \ldots 0.9$) and of β_{N} was achieved until the end of the control phase, with a flat-top β_{N} target of 2.1, and also in a discharge with a flat-top β_{N} target of 2.5 where an $m/n = 2/1$ MHD mode (NTM) appeared around $t = 2.3\,\mathrm{s}$. Despite this mode, simultaneous $\Psi(x)$ and β_{N} control was achieved starting at $t = 1\,\mathrm{s}$, and a nice regulated steady state was obtained between $t = 4\,\mathrm{s}$ and $t = 5.5\,\mathrm{s}$ at which control was switched off. However, in another discharge in which control started at $t = 0.5\,\mathrm{s}$ with the same final β_{N} target of 2.5, this $m/n = 2/1$ NTM locked, and this led to the early termination of the discharge. Additional real-time NTM control may therefore be necessary for achieving high-β_{N} steady-state plasmas in a reliable and reproducible way, but MHD instability avoidance should also be included, to any possible extent, among the missions of magneto-kinetic profile control.

Finally, optimal feedback control of the safety factor profile was attempted using an extension of the same control algorithm, with appropriate cost objectives defined in terms of its inverse, $\bar{\iota}(x) = 1/q(x)$. In these experiments, the off-axis beam actuator was used and the target was defined as a broad flat q-profile between $x = 0$ and $x \approx 0.6$, with a minimum value, $q_{\mathrm{min}} = 1.7$, typical of those that are sought for high performance AT scenarios. Starting from $t = 1\,\mathrm{s}$, during current ramp-up, the controller satisfactorily tracked the target profile while the current was raised up to 1.2 MA and maintained for about one second at this level, until control was lost due to a technical fault in the control of the ohmic coil current and plasma loop voltage.

Altogether, these experiments have demonstrated effective current profile control and a proof of principle of a simultaneous magnetic and kinetic control using a two-time-scale algorithm. They provide an important basis for further progress, and more extensive experimental investigations and numerical simulations will be carried out in the future. This research should lead to the rapid development of integrated plasma control for advanced scenarios in DIII-D and provide valuable input for the design of advanced plasma controllers in ITER.

Acknowledgments

References

[1] Holcomb C.T. *et al* 2009 *Phys. Plasmas* **16** 056116
[2] Ferron J.R. *et al* 2011 *Nucl. Fusion* **51** 063026
[3] Oyama N. and the JT-60 Team 2009 *Nucl. Fusion* **49** 104007
[4] Litaudon X. *et al* 2011 *Nucl. Fusion* **51** 073020
[5] Barton J.E. *et al* 2012 *Proc. 24th IAEA Fusion Energy Conf. (San Diego, CA, 2012)* paper EX/P2–09
[6] Felici F. *et al* 2012 *Proc. 24th IAEA Fusion Energy Conf. (San Diego, CA, 2012)* paper EX/P3-12
[7] Moreau D. *et al* 2008 *Nucl. Fusion* **48** 106001
[8] Moreau D. *et al* 2011 *Nucl. Fusion* **51** 063009
[9] Wehner W. *et al* 2012 *Proc. American Control Conf. (Montreal, Canada, 2012)* p 5049
[10] Shi W. *et al* 2012 *Proc. American Control Conf. (Montreal, Canada, 2012)* p 5037
[11] Ljung L. 1999 *System Identification: Theory for the User* (Upper Saddle River, NJ: Prenctice Hall PTR)
[12] Kokotovitch P.V. *et al* 1986 *Singular Perturbation Methods in Control: Analysis and Design* (London: Academic)
[13] Liu F., Moreau D., Artaud J.F., Garcia J. and Nouailletas R. 2012 Model-based magnetic and kinetic control of ITER scenarios *Proc. 39th EPS Conf. on Plasma Physics (Stockholm, Sweden, 2012)* P1.063 http://ocs.ciemat.es/epsicpp2012pap/html/contrib.html
[14] Ferron J.R., Penaflor B.G., Walker M.L., Moller J.M. and Butner D. 1996 *Proc. 16th IEEE/NPSS Symp. on Fusion Engineering (Champaign, Illinois)* (Piscataway: Institute of Electrical and Electronics Engineers Inc.) vol 2, p 870
[15] Ray W.H. 1981 *Advanced Process Control* (New York: McGraw-Hill)
[16] Lao L.L., St. John H., Stambaugh R.D., Kellman A.G. and Pfeiffer W. 1985 *Nucl. Fusion* **25** 1611
[17] Ferron J.R. *et al* 2006 *Nucl. Fusion* **46** L13
[18] Kolemen E., Welander A.S., LaHaye R.J., Eidietis N.W., Humphreys D.A., Lohr J., Noraky S., Penaflor B.G., Prater R. and Turco F. 2012 State-of-the-art neoclassical tearing mode control in DIII-D using real-time steerable electron cyclotron current drive launchers *Proc. of the 24th IAEA Fusion Energy Conf. (San Diego, CA, 2012)* Paper PD/1-1